

## Article

# Liquid-Phase Deposition Synthesis of ZIF-67-Derived Synthesis of $\text{Co}_3\text{O}_4@\text{TiO}_2$ Composite for Efficient Electrochemical Water Splitting

Zaffar Ahmed Shaikh <sup>1,\*</sup>, Asif Ali Laghari <sup>2</sup>, Oleg Litvishko <sup>3</sup>, Valery Litvishko <sup>3</sup>, Tatyana Kalmykova <sup>3</sup> and Artur Meynkhard <sup>4</sup>

<sup>1</sup> Faculty of Computer Science & Information Technology, Benazir Bhutto Shaheed University, Lyari, Karachi 75660, Pakistan

<sup>2</sup> Department of Computer Science, Sindh Madressatul Islam University, Karachi 75500, Pakistan; asif.laghari@smiu.edu.pk

<sup>3</sup> Plekhanov Russian University of Economics, 117997 Moscow, Russia; s\_124@mail.ru (O.L.); s\_543@mail.ru (V.L.); s\_753@mail.ru (T.K.)

<sup>4</sup> Department of Financial Markets and Banks, Financial University under the Government of the Russian Federation, 125993 Moscow, Russia; meynkhard@ya.ru

\* Correspondence: zashaikh@bbsul.edu.pk; Tel.: +92-3337-113-817

**Abstract:** In this article, a novel  $\text{Co}_3\text{O}_4@\text{TiO}_2$  composite is synthesized by applying two-step methods. ZIF-67 is synthesized and used as a template for the synthesis of the composite. The composite is designed by using the effective photocatalytic properties of  $\text{Co}_3\text{O}_4$  and  $\text{TiO}_2$ . The resulting synthesized composite is supposed to offer superior properties compared to their counterparts. The synthesized  $\text{Co}_3\text{O}_4@\text{TiO}_2$  composite is characterized by powder X-ray diffraction (PXRD), Brunauer–Emmet–Teller (BET), atomic force microscopy (AFM), scanning electron microscopy (SEM), and transmission electron microscopy (TEM). Electrochemical water splitting, including hydrogen evolution reaction (HER) and oxygen evolution reaction (OER) studies on the  $\text{Co}_3\text{O}_4@\text{TiO}_2$  composite, is evaluated by cyclic voltammetry (CV) and linear sweep voltammetry (LSV) analysis in a 2M aqueous KOH electrolyte. The current generation stability of these samples is deliberated by chronoamperometric measurements. It is observed, from LSV results at a 1 mV/s scan rate, that metal oxides incorporated on other metal oxides have a higher current density and lower onset potential as compared to pure metal oxides. From the obtained results, it has become evident that synthesized studies on the  $\text{Co}_3\text{O}_4@\text{TiO}_2$  composite possess significant potential for electrochemical water splitting with the lowest onset potential, highest current density, better OER, and HER activity.

**Keywords:** water splitting; HER; OER;  $\text{Co}_3\text{O}_4@\text{TiO}_2$  composite; current density; the onset potential



**Citation:** Shaikh, Z.A.; Laghari, A.A.; Litvishko, O.; Litvishko, V.; Kalmykova, T.; Meynkhard, A. Liquid-Phase Deposition Synthesis of ZIF-67-Derived Synthesis of  $\text{Co}_3\text{O}_4@\text{TiO}_2$  Composite for Efficient Electrochemical Water Splitting. *Metals* **2021**, *11*, 420. <http://doi.org/10.3390/met11030420>

Academic Editors: Thomas Gries and Petros E. Tsakiridis

Received: 20 January 2021

Accepted: 28 February 2021

Published: 4 March 2021

**Publisher's Note:** MDPI stays neutral with regard to jurisdictional claims in published maps and institutional affiliations.



**Copyright:** © 2021 by the authors. Licensee MDPI, Basel, Switzerland. This article is an open access article distributed under the terms and conditions of the Creative Commons Attribution (CC BY) license (<https://creativecommons.org/licenses/by/4.0/>).

## 1. Introduction

Currently, the whole world is facing serious energy and global warming crises. Both these issues are inter-related and closely associated with the consumption of fossil fuels. A high consumption of fossil fuels means its resources are in fast decline [1]. This also means a higher production of carbon dioxide, which is the main contributor to global warming. Global warming is increasing every day, and the rapid decline in natural petroleum sources has been observed, increasing the interest in developing new sources of clean and sustainable energy [2]. Moreover, the use of fossil fuels is a huge burden on the economy of lower-income countries. Considering these problems, researchers are working on alternative sources of energy [3]. Renewable energy is a promising solution to all of the above-mentioned problems. There are different ways to generate energy, but hydrogen is cheap, efficient, and an environmentally friendly candidate [4]. The gravimetric energy density of hydrogen is a little higher than petroleum ( $44 \text{ kJ}\cdot\text{g}^{-1}$ ) [5]. Due to its unique properties, such as being easy to store and transport, and the ability to be used without

producing any harmful byproducts, hydrogen is considered an efficient source of energy. Energy production by water splitting into hydrogen gas provides a hopeful solution in the future [6]. A notable study on the design and application of different photocatalytic reactors for water splitting has been carried out for many years. Semiconductors and photosensitizers are used as common photocatalysts, but lower hydrogen yield is still a major challenge for industrial-scale production [7].

Several nanomaterials and their combinations are used as catalysts for hydrogen production via water splitting [8,9]. Metal oxides [10], their composites with other metal oxides [11], metal oxide composites with carbon-based materials [12], doped metal oxides [13], perovskites [14], carbon-based composites [15], metal–organic frameworks [16], metal nanosheets [17], and many other combinations [18,19] have been recently reported for water oxidation. Due to the unique properties of metal–organic frameworks (MOFs), research and scientific breakthroughs have attracted attention [19,20]. MOFs are efficient photocatalysts for water splitting [21,22]. Furthermore, different types of materials, nanomaterials including metal/metal oxide, carbon-based materials, polymers, and composites can be attached with MOFs to enhance the photocatalytic activity of MOFs and can be used for different applications including water splitting [23–26]. Metal oxide composites with other metal oxides possess some fascinating properties including high surface area, improved catalytic properties, and better conductivity [27]. By improving the charge transfer between electrode and electrolyte, the production of hydrogen can be improved and the whole process can be made faster by some modifications in the catalysts [28,29]. This can be efficiently done by transferring electrons (photogenerated electrons). By using this route, charge separation is increased, leading to the higher production of H<sub>2</sub> [30].

The rapid and greater attention of researchers toward metal oxides is explained by their wide range, versatile chemistry, cheap availability, and high stability [31,32]. Metal oxide composites are commonly used as sensors [33], separation science [34], supercapacitors [35], optoelectronic devices [36], and in Li-ion batteries [37]. Metal oxides such as Co<sub>3</sub>O<sub>4</sub>, Fe<sub>2</sub>O<sub>3</sub>, MnO<sub>2</sub>, NiO, and CuO are commonly used in water splitting as well. These metal oxides are used purely, as well as in combination, with other metal oxides, carbon-based materials, MOFs, and doped materials. Initially, noble metal-based catalysts were used for water oxidation for both oxidation evolution reaction (OER) and hydrogen evolution reaction (HER) [38]. However, the recent trend has shifted toward nonnoble metal catalysis due to its low cost, easy availability, and multifunctional characteristics [39,40].

In the present work, a MOF template synthesis of the Co<sub>3</sub>O<sub>4</sub>@TiO<sub>2</sub> composite is done. Co<sub>3</sub>O<sub>4</sub> is synthesized from the calcination of ZIF-67. Multi-layer deposition of TiO<sub>2</sub> on Co<sub>3</sub>O<sub>4</sub> is done via the facile liquid-phase deposition synthesis method. The prepared composite is used as an efficient catalyst for electrochemical water splitting. Titanium oxide contains unique surface characteristics, which are very useful in electrochemical catalysis [41,42]. The Co<sub>3</sub>O<sub>4</sub>@TiO<sub>2</sub> composite shows promising efficiency for electrochemical catalysis for hydrogen production.

## 2. Materials and Methods

### 2.1. Chemical and Reagents

2-Methylimidazole, boric acid (H<sub>3</sub>BO<sub>3</sub>) (99%), Co(NO<sub>3</sub>)<sub>2</sub>·6H<sub>2</sub>O, ammonium hexafluorotitanate ((NH<sub>4</sub>)<sub>2</sub>TiF<sub>6</sub>) (99%), *N,N*-dimethyl formamide (DMF, 99.8%), methanol (CH<sub>3</sub>OH, 99.9%), sodium hydroxide [NaOH, 97%], and ethanol [CH<sub>3</sub>CH<sub>2</sub>OH 95%] were purchased from Sigma Aldrich (St. Louis, MO, USA). Cobalt acetate tetrahydrate [C<sub>4</sub>H<sub>6</sub>CoO<sub>4</sub>·4H<sub>2</sub>O] and ammonia solution [NH<sub>4</sub>OH (28%)] were obtained from Merck. Deionized water was obtained from the Milli-Q water purification system (Merck Millipore, Germany). All the chemicals and reagents were of analytical grade and used without any further purification.

## 2.2. Synthesis of ZIF-67 and $\text{Co}_3\text{O}_4$

First, 1.164 g of cobalt nitrate (3.9 mmol) was dissolved in 25 mL of ethanol and 1.31 g of 2-methylimidazole (14.8 mmol) was dissolved in 25 mL of methanol. Both solutions were mixed and sonicated for ten minutes. Then, the mixture was kept at room temperature overnight. The obtained purple-colored product was centrifuged, washed with ethanol, deionized in water, and then vacuum-dried for 6 h at 60 °C. The dried product was ZIF-67, which was heated to 450 °C in a temperature-programmed electric furnace (Memmert, Büchenbach, Germany) for 2 h at a rate of 2 °C min<sup>-1</sup>. The purple color of the product was converted to a dark-colored powder.

Then, 0.50 g of cobalt acetate tetrahydrate was dissolved in 25 mL of de-ionized water, followed by the addition of 2.5 mL of ammonia solution (25%). The mixture was agitated at high speeds for 15 min, followed by vigorous stirring for 10 min. The hydrothermal reaction was carried out in a Teflon-lined stainless autoclave in an electrical oven (Memmert, Büchenbach, Germany) at 150 °C for 6 h. After cooling to room temperature, the obtained product ( $\text{Co}_3\text{O}_4$ ) was washed with ethanol and water, and vacuum-dried at 60 °C for 4 h [43].

## 2.3. Synthesis of $\text{Co}_3\text{O}_4@\text{TiO}_2$ Composite

Multi-layer deposition of  $\text{TiO}_2$  on  $\text{Co}_3\text{O}_4$  particles was done by the liquid-phase deposition (LPD) method. Finally, as-synthesized  $\text{Co}_3\text{O}_4$  nanoparticles were suspended in a 50 mL solution of ammonium hexafluorotitanate (0.1 M) and a boric acid solution (0.3 M). The mixture was vigorously stirred for 15 min to form a homogenous solution. To remove oxygen from the solution mixture, it was kept in a vacuum at 35 °C for 1 h. Then, the solution was heated for 12 h on a hot plate with a magnetic stirrer. The obtained  $\text{Co}_3\text{O}_4@\text{TiO}_2$  composite was washed with deionized water and vacuum-dried in an electric oven for 6 h at 60 °C. To obtain multi-layers of  $\text{TiO}_2$  on  $\text{Co}_3\text{O}_4$  particles, the process was repeated three times [44].

## 2.4. Characterization of $\text{Co}_3\text{O}_4@\text{TiO}_2$ Composite

The sample was analyzed with a Shimadzu XRD diffractometer (Bruker D8 Advance, Karlsruhe, Germany) at room temperature, using Cu-K $\alpha$  radiation ( $\lambda = 0.15406$  nm) in the range of  $2\theta$  between 5° and 80° with a step size of 0.03° and a scan speed of 1°/min. The topography and morphology of the  $\text{Co}_3\text{O}_4@\text{TiO}_2$  composite were investigated by using scanning electron microscopy (SEM, JEOL JSM-7900F Japan). SEM images were obtained by using a Philips XL30 Environmental SEM. UV-Vis spectra were recorded on a Shimadzu UV-2600 (UV-Visible spectrophotometer, Shimadzu UV 3600, Japan) in the range of 200–900 nm at room temperature. The sample was analyzed using a Quantachrome NOVA 2200 (Quantachrome, Japan) in liquid nitrogen at 77 K to determine the Brunauer–Emmet–Teller (BET) value of the sample.

## 2.5. Electrochemical Measurements

Three electrode cells (Uniscan instruments 3100 Potentiostat/Galvanostat, Gamry Reference 3000 w/AE, UK) were used for the photoelectrochemical measurements for OER and HER. The electrochemical system was equipped with conventional three-electrode cells. The  $\text{Co}_3\text{O}_4@\text{TiO}_2$  composite was deposited on nickel foam as a working electrode, the counter electrode was a simple Pt-wire, and the reference electrode used was Ag/AgCl (3M aq. KCl). All the measurements, both OER and HER, were performed in an alkaline medium consisting of a 2M solution of KOH. To prepare the working electrodes, the slurry of metal oxide nanoparticles was pasted on a cleaned and nickel foam (1 cm × 1 cm) and dried in an oven at 50 °C overnight. The scan rate during CV measurements was set at 100 mV/s, while LSV measurements were carried out at a 1 mV/s scan rate. A constant

voltage of 1.5 V was maintained during chronoamperometry. The acquired data were processed using the following equations:

$$E_{\text{RHE}} = E_{\text{Ag/AgCl/Sat. KCl}} + 0.059 \text{ pH} + 0.197 \quad (1)$$

The OER and HER overpotential ( $\eta$ ) was calculated by using the following equations:

$$\text{For OER, } \eta = E_{\text{RHE}} - 1.23 \quad (2)$$

$$\text{For HER, } \eta = 0 - E_{\text{RHE}} \quad (3)$$

The Tafel slope was calculated using the Tafel plot with the following equation:

$$\eta = a + b \log j \quad (4)$$

where  $\eta$  is the overpotential,  $b$  is the Tafel slope, and  $j$  is the current density.

### 3. Results and Discussion

#### 3.1. Characterization of $\text{Co}_3\text{O}_4@\text{TiO}_2$ Composite

PXRD is a powerful technique to study the diffraction patterns of crystalline materials. PXRD patterns of the  $\text{Co}_3\text{O}_4@\text{TiO}_2$  composite are shown in Figure 1A. Characteristic peaks of the composite appeared at  $31^\circ$ ,  $37^\circ$ ,  $45^\circ$ ,  $48^\circ$ ,  $50^\circ$ ,  $59^\circ$ , and  $65^\circ$ , corresponding to 101, 110, and 220 facets showing the diffraction peaks of  $\text{Co}_3\text{O}_4$  and  $\text{TiO}_2$  [45]. All these peaks are sharp and well-defined, which indicates the crystalline nature of the composite. BET analysis was carried out to access the surface area of the  $\text{Co}_3\text{O}_4@\text{TiO}_2$  composite. The adsorption–desorption isotherm for the BET surface area is given in Figure 1B. The obtained surface of the material was  $391 \text{ m}^2/\text{g}$ , which is overwhelmingly high. This high surface area could be a key factor in determining the catalytic performance of the material. The surface areas of  $\text{Co}_3\text{O}_4$  and  $\text{TiO}_2$  were 132 and  $197 \text{ m}^2/\text{g}$ , respectively. The AFM image of the  $\text{Co}_3\text{O}_4@\text{TiO}_2$  composite is shown in Figure 1C. The image shows that the particles were semispherical and the estimated particle size was around 20–40 nm. The SEM image of the  $\text{Co}_3\text{O}_4@\text{TiO}_2$  composite is shown in Figure 1D, which justifies the morphology and shape of the particles. TEM analysis was also carried out to study the inner morphology of the composite. The results show the nanosize of the particle. The TEM image also shows the combination of two different types of metal oxides in a single structure with a high degree of crystallinity (Figure 1E).

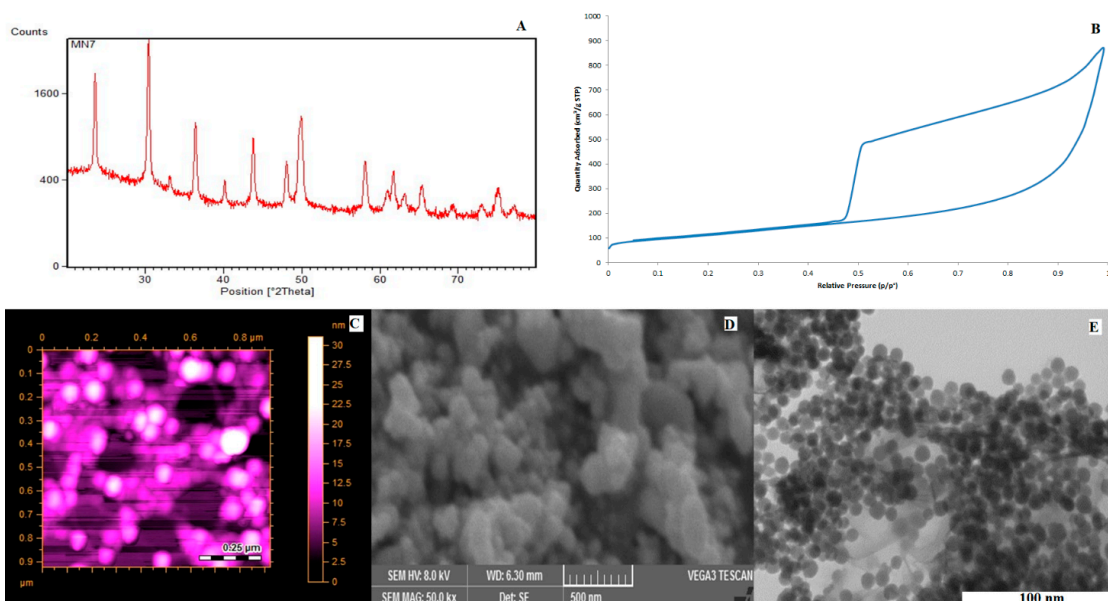


**Figure 1.** (A) XRD, (B) BET, (C) AFM, (D) SEM, and (E) TEM of the  $\text{Co}_3\text{O}_4@\text{TiO}_2$  composite.

The efficiency of the catalyst that operates in the visible region depends on the amount of visible light they absorb in the visible band. Thus, to evaluate the performance of all these prepared compounds, UV-Vis spectroscopy was utilized and their optical properties were examined using this technique. The results are given below in Figure 2a.  $\lambda_{\max}$  at 226 and 331 nm was obtained in the case of the  $\text{Co}_3\text{O}_4/\text{TiO}_2$  composite. This one did not show absorption peaks in the visible region. The absorption edge of  $\text{Co}_3\text{O}_4$  was extended to the visible region as well. The bandgap of the  $\text{Co}_3\text{O}_4$ ,  $\text{TiO}_2$ , and  $\text{Co}_3\text{O}_4/\text{TiO}_2$  composites was determined by the Tauc plot (Figure 2b) by extrapolating  $(\alpha h\nu)^2$  and the tangent of the photon energy. Furthermore, by using the Tauc plot, the calculated values of bandgaps were 1.27, 2.63, and 2.51 eV. The bandgap became low by composite formation, so absorption in the visible region increased. A lower bandgap results in the increase in the charge separation and reduction in the electron–hole pair combination [46], and all these improved properties enhance the water-splitting ability of the catalyst.

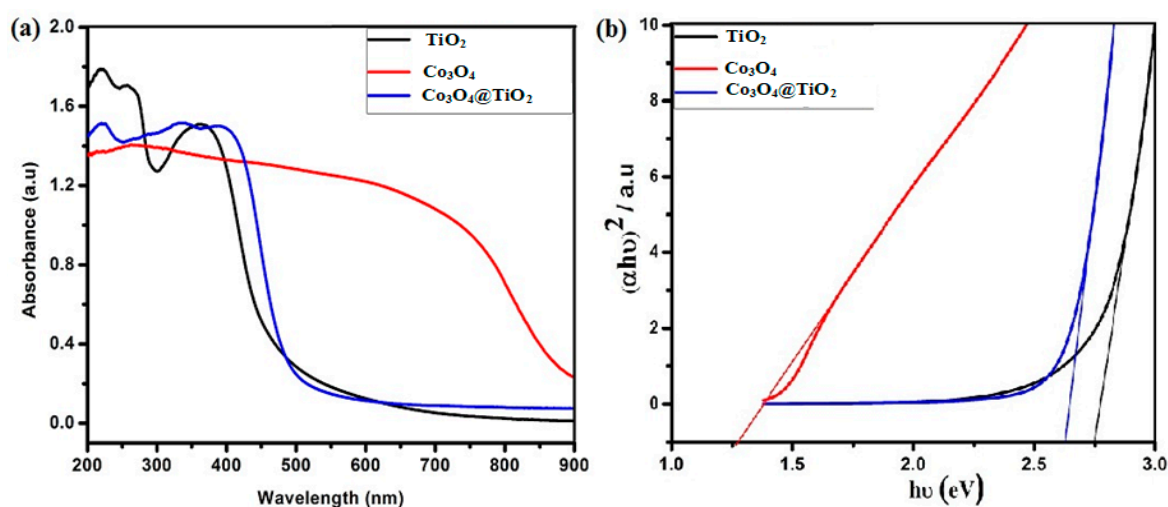


Figure 2. (a) UV-Vis spectra; (b) Tauc plot of  $\text{Co}_3\text{O}_4$ ,  $\text{TiO}_2$ , and  $\text{Co}_3\text{O}_4/\text{TiO}_2$  composite.

### 3.2. Electrocatalytic Hydrogen Evolution Reaction by $\text{Co}_3\text{O}_4/\text{TiO}_2$ Composite

Electrocatalytic activities of the  $\text{Co}_3\text{O}_4$ ,  $\text{TiO}_2$ , and  $\text{Co}_3\text{O}_4/\text{TiO}_2$  composites for the hydrogen evolution reaction (HER) were evaluated by nickel foam using a three-electrode system. Cyclic voltammetry (CV) and linear sweep voltammetry (LSV) were used for the evaluation of HER activities in an alkaline electrolyte solution. Cyclic voltammetry experiments were performed in the potential range of  $-0.4$  to  $1.0$  V vs. RHE (reversible hydrogen electrode). The  $\text{Co}_3\text{O}_4$ ,  $\text{TiO}_2$ , and  $\text{Co}_3\text{O}_4/\text{TiO}_2$  composites were all tested for HER activity and the  $\text{Co}_3\text{O}_4/\text{TiO}_2$  composite demonstrated the lowest onset potential (Figure 3a). These results show that the combination of  $\text{Co}_3\text{O}_4$  and  $\text{TiO}_2$  in a binary composite demonstrated better HER performance as compared to individual counterparts. The maximum current density was also obtained using the  $\text{Co}_3\text{O}_4/\text{TiO}_2$  composite ( $-19.93 \text{ mAcm}^{-2}$ ) in comparison to  $\text{Co}_3\text{O}_4$  ( $-9.71 \text{ mAcm}^{-2}$ ) and  $\text{TiO}_2$  ( $-7.13 \text{ mAcm}^{-2}$ ). LSV measurements were also carried out to further evaluate the HER activities of the  $\text{Co}_3\text{O}_4$ ,  $\text{TiO}_2$ , and  $\text{Co}_3\text{O}_4/\text{TiO}_2$  composite (Figure 3b). LSV measurements were recorded at a  $1 \text{ mV/s}$  scan rate. The negative current density increased in response to the cathodic applied potential vs. RHE. LSV results demonstrate that the  $\text{Co}_3\text{O}_4/\text{TiO}_2$  composite showed the lowest onset potential compared to individual  $\text{Co}_3\text{O}_4$  and  $\text{TiO}_2$ . An overpotential of  $-10 \text{ mAcm}^{-2}$  was always set as a benchmark for water splitting. The lowest overpotential ( $153 \text{ mV}$ ) was achieved for the  $\text{Co}_3\text{O}_4/\text{TiO}_2$  composite, while  $\text{Co}_3\text{O}_4$  and  $\text{TiO}_2$  showed  $196$  and  $212 \text{ mV}$ . This shows that the formation of the composite resulted in a lower onset potential. The  $\text{Co}_3\text{O}_4/\text{TiO}_2$  composite also had a lower overpotential than  $\text{Co}_3\text{O}_4$  and  $\text{TiO}_2$  (Figure 3c).

The Tafel slope is another important parameter in water splitting studies, which was calculated by the linear region of the LSV curve. The Tafel slope of the  $\text{Co}_3\text{O}_4$ ,  $\text{TiO}_2$ , and

$\text{Co}_3\text{O}_4@\text{TiO}_2$  composites is shown in Figure 3d. Among the synthesized materials, the  $\text{Co}_3\text{O}_4@\text{TiO}_2$  composite also demonstrated the lowest Tafel slope (81  $\text{mVdec}^{-1}$ ), while the observed Tafel slope values for  $\text{Co}_3\text{O}_4$  and  $\text{TiO}_2$  were 181 and 201  $\text{mVdec}^{-1}$ , respectively. These results further indicate the better electron transfer system of the  $\text{Co}_3\text{O}_4@\text{TiO}_2$  composite as compared to pure  $\text{Co}_3\text{O}_4$  and  $\text{TiO}_2$ . This faster electron transfer system facilitated the HER activity at the electrode–electrolyte interface. These results indicate that the evolution of the hydrogen after electrochemical catalysis followed the Volmer–Heyrovsky mechanism, which usually happens at Tafel slope values between 50 and 120  $\text{mVdec}^{-1}$ . However, to carry out HER in an alkaline solution, a slightly higher overpotential value is also required for the generation of protons. This happens due to the oxidation of anions of water or hydroxide at the anode as there are no protons available in the basic medium.

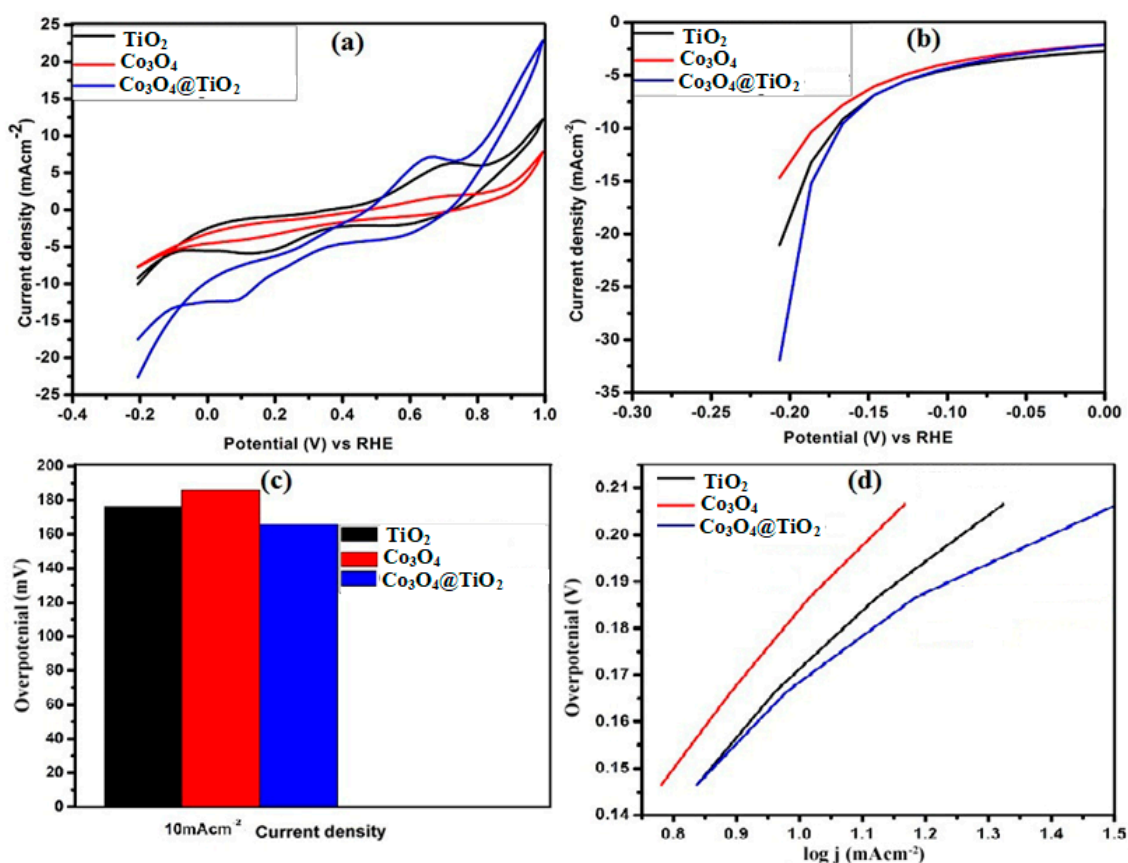


**Figure 3.** (a) CV, (b) linear sweep voltammetry (LSV) curves, (c) overpotential, and (d) Tafel plot of  $\text{Co}_3\text{O}_4$ ,  $\text{TiO}_2$ , and  $\text{Co}_3\text{O}_4@\text{TiO}_2$  composite.

### 3.3. Electrocatalytic Oxygen Evolution Reaction (OER) Studies

The oxygen evolution reaction (OER) capability of synthesized materials was also studied by LSV and CV using the same three-electrode systems in an alkaline medium. The potential range for OER was between 1.0 and 1.6 V vs. RHE. Some pre-oxidative peaks appeared in the CV curves between 1.24 and 1.41 V vs. RHE (Figure 4a). These pre-oxidative peaks formed due to the oxidation of metals on the electrode surface and, as a result, M-OOH formed on the surface of working electrodes. After the pre-oxidative peaks, actual catalytic peaks could be seen, which appeared at 1.47, 1.39, and 1.31 V for  $\text{Co}_3\text{O}_4$ ,  $\text{TiO}_2$ , and the  $\text{Co}_3\text{O}_4@\text{TiO}_2$  composite, respectively. These peaks indicate oxygen formation, which evolved in the form of bubbles. As discussed previously in the case of HER, OER results also show that the  $\text{Co}_3\text{O}_4@\text{TiO}_2$  composite had the lowest onset potential and highest current density ( $23.91\text{ mAcm}^{-2}$ ) as compared to  $\text{Co}_3\text{O}_4$  ( $13.21\text{ mAcm}^{-2}$ ) and  $\text{TiO}_2$  ( $11.576\text{ mAcm}^{-2}$ ).

A similar trend was observed in the case of LSV measurements as well. LSV analyses were carried out at a  $1 \text{ mVs}^{-1}$  scan rate and potential range of 1.0 to 1.6 V (Figure 4b). These results also verify the superior and improved catalytic performance of the  $\text{Co}_3\text{O}_4@\text{TiO}_2$  composite. The lowest overpotential 269 mV for  $10 \text{ mAcm}^{-2}$  with current density was achieved by the  $\text{Co}_3\text{O}_4@\text{TiO}_2$  composite compared to  $\text{Co}_3\text{O}_4$  (309 mV) and  $\text{TiO}_2$  (313 mV). The lower overpotential at  $10 \text{ mAcm}^{-2}$  was also observed for the  $\text{Co}_3\text{O}_4@\text{TiO}_2$  composite, which is better than several other materials (Figure 4c). Tafel slope values and water oxidation electrochemical kinetics of all three materials are shown in Figure 4d. The  $\text{Co}_3\text{O}_4@\text{TiO}_2$  composite demonstrated the lowest Tafel slope ( $106 \text{ mV dec}^{-1}$ ), while  $\text{Co}_3\text{O}_4$  and  $\text{TiO}_2$  showed 161 and  $196 \text{ mV dec}^{-1}$ , respectively. These results further confirm the superior performance of the  $\text{Co}_3\text{O}_4@\text{TiO}_2$  composite for OER as well. This may be attributed to the formation of the metal oxy-hydroxide intermediate, which further deprotonates, resulting in the oxygen evolution.

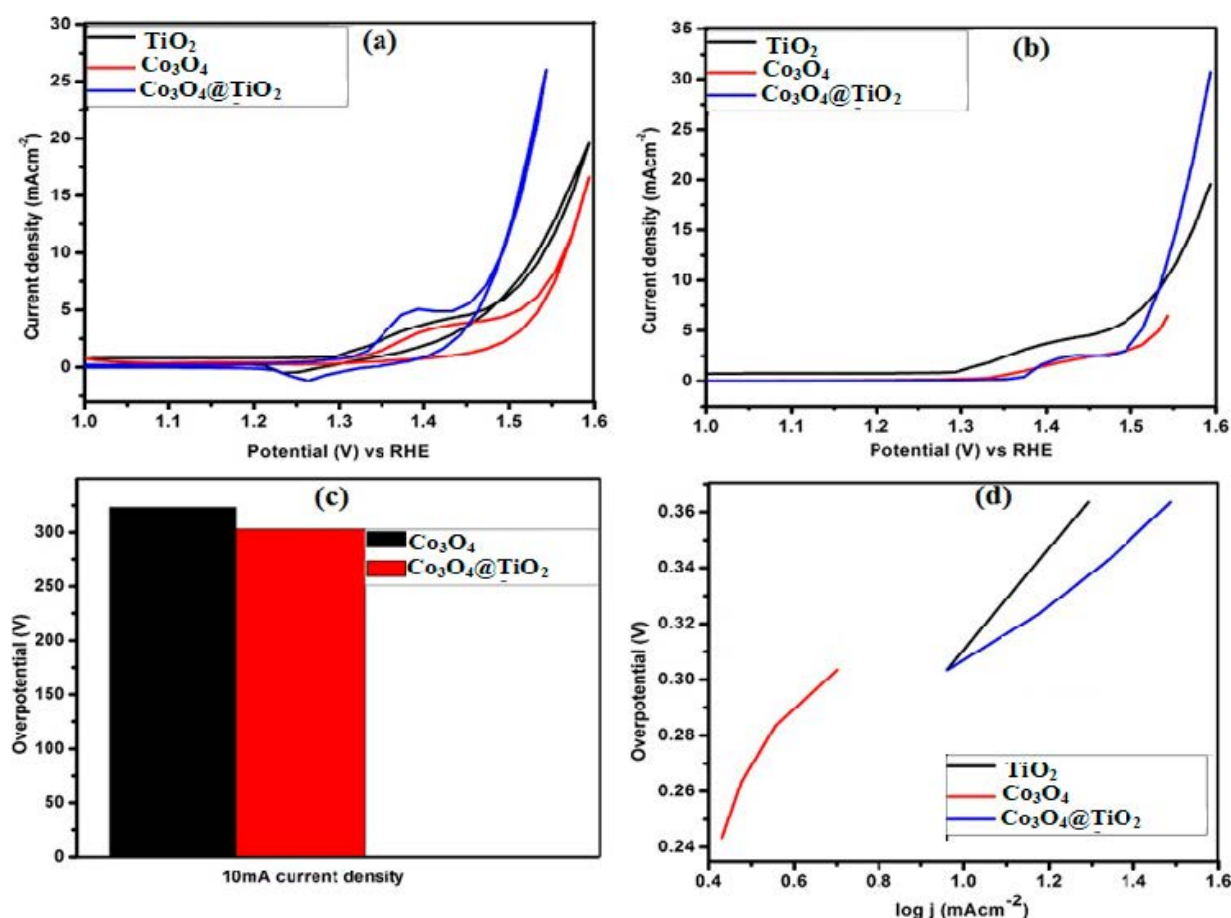
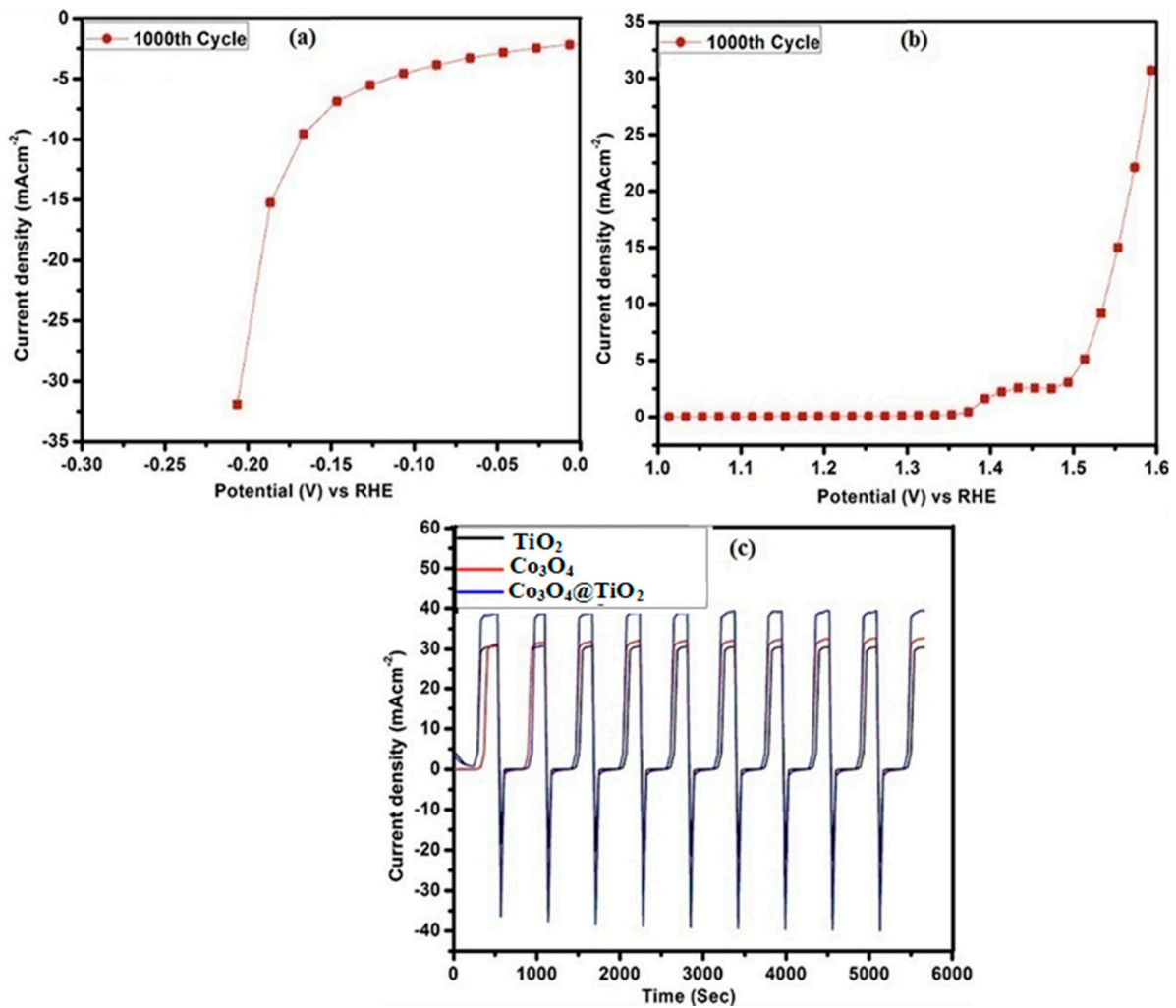


Figure 4. (a) CV, (b) LSV curves, (c) overpotential, and (d) Tafel plot for  $\text{Co}_3\text{O}_4$ ,  $\text{TiO}_2$ , and  $\text{Co}_3\text{O}_4@\text{TiO}_2$  composite.

The stability of the catalyst is an important factor for scaled-up application. Owing to the superior performance of the  $\text{Co}_3\text{O}_4@\text{TiO}_2$  composite, long-term stability was evaluated by chronoamperometry and linear sweep voltammetry. LSV stability of the  $\text{Co}_3\text{O}_4@\text{TiO}_2$  composite was studied in an alkaline medium for 1000 cycles (Figure 5a,b). No significant change was observed from the 1st cycle to the 1000th. These findings demonstrate the excellent stability of the catalyst in alkaline conditions. As all the cycles were perfectly superimposable, this shows that the material can be used multiple times, reducing costs. Chronoamperometric measurements for the  $\text{Co}_3\text{O}_4@\text{TiO}_2$  composite were carried out for 6000 s to further verify the stability and reusability of the catalyst (Figure 5c). The linear curve indicates that the material was stable for a longer time with constant current density. Thus, the higher stability confirms the better performance of the composite material for

water oxidation. The results show that there was no significant change over time in the time vs. current density curves.



**Figure 5.** Stability studies. (a,b) 1st and 1000th LSV cycle, respectively, and (c) chronoamperometry of Co<sub>3</sub>O<sub>4</sub>@TiO<sub>2</sub> composite at 1.5 V for 6000 s.

#### 4. Conclusions

In this work, we successfully synthesized a MOF-derived Co<sub>3</sub>O<sub>4</sub>@TiO<sub>2</sub> composite by a two-step process. Co<sub>3</sub>O<sub>4</sub> was synthesized by using the ZIF-67 template via the hydrothermal method, followed by liquid-phase deposition of multi-layered TiO<sub>2</sub>. The formation of the composite effectively enhanced the charge partition, decreased the energy gap, and upgraded the OER and HER. In all of these prepared compounds, the Co<sub>3</sub>O<sub>4</sub>@TiO<sub>2</sub> composite displayed superior properties because of the narrow energy gap, minimal surface exposure, and extra active margins. The materials demonstrated excellent stability as well, which is equally applicable to HER and OER. Composite formation enhanced the water oxidation process during HER and OER. These prepared materials showed better stability at different pH conditions. This property makes them excellent electrochemical catalysts for water splitting.

**Author Contributions:** Conceptualization, Z.A.S., A.A.L., O.L. and T.K.; methodology, Z.A.S. and V.L.; software, Z.A.S., T.K. and O.L.; validation, A.A.L. and A.M.; formal analysis, Z.A.S. and O.L.; investigation, V.L. and A.M.; resources, Z.A.S., O.L., T.K. and A.M.; data curation, Z.A.S. and A.A.L.; writing—original draft preparation, Z.A.S.; writing—review and editing, Z.A.S., A.A.L., O.L. and A.M.; visualization, O.L. and V.L.; supervision, Z.A.S.; project administration, Z.A.S., A.A.L. and O.L.; funding acquisition, Z.A.S., T.K., V.L. and A.M. All authors have read and agreed to the published version of the manuscript.

**Funding:** This research received no external funding.

**Institutional Review Board Statement:** Not applicable.

**Informed Consent Statement:** Not applicable.

**Data Availability Statement:** Data sharing not applicable.

**Conflicts of Interest:** The authors declare no conflict of interest.

## References

1. Peter, S.C. Reduction of CO<sub>2</sub> to Chemicals and Fuels: A Solution to Global Warming and Energy Crisis. *ACS Energy Lett.* **2018**, *3*, 1557–1561. [[CrossRef](#)]
2. Martins, F.; Felgueiras, C.; Smitkova, M.; Caetano, N. Analysis of Fossil Fuel Energy Consumption and Environmental Impacts in European Countries. *Energies* **2019**, *12*, 964. [[CrossRef](#)]
3. Pandey, A.K.; Rahim, N.A.; Hasanuzzaman, M.; Pant, P.C.; Tyagi, V.V. Solar Photovoltaics (PV): A Sustainable Solution to Solve Energy Crisis. In *Green Technologies and Environmental Sustainability*; Springer: Berlin/Heidelberg, Germany, 2017; pp. 157–178.
4. Hosseini, S.E.; Wahid, M.A. Hydrogen from solar energy, a clean energy carrier from a sustainable source of energy. *Int. J. Energy Res.* **2020**, *44*, 4110–4131. [[CrossRef](#)]
5. Wang, X.; Meng, Q.; Gao, L.; Jin, Z.; Ge, J.; Liu, C.; Xing, W. Recent progress in hydrogen production from formic acid de-composition. *Int. J. Hydrog. Energy* **2018**, *43*, 7055–7071. [[CrossRef](#)]
6. Kaur, M.; Pal, K. Review on hydrogen storage materials and methods from an electrochemical viewpoint. *J. Energy Storage* **2019**, *23*, 234–249. [[CrossRef](#)]
7. Abdalla, A.M.; Hossain, S.; Nisfindy, O.B.; Azad, A.T.; Dawood, M.; Azad, A.K. Hydrogen production, storage, transportation and key challenges with applications: A review. *Energy Convers. Manag.* **2018**, *165*, 602–627. [[CrossRef](#)]
8. Bhosale, R.; Kumar, A.; Almomani, F.; Gupta, R.B. Solar thermochemical ZnO/ZnSO<sub>4</sub> water splitting cycle for hydrogen production. *Int. J. Hydrog. Energy* **2017**, *42*, 23474–23483. [[CrossRef](#)]
9. Hisatomi, T.; Domen, K. Reaction systems for solar hydrogen production via water splitting with particulate semiconductor photocatalysts. *Nat. Catal.* **2019**, *2*, 387–399. [[CrossRef](#)]
10. Yang, Y.; Niu, S.; Han, D.; Liu, T.; Wang, G.; Li, Y. Progress in Developing Metal Oxide Nanomaterials for Photoelectrochemical Water Splitting. *Adv. Energy Mater.* **2017**, *7*, 1700555. [[CrossRef](#)]
11. Long, X.; Lin, H.; Zhou, D.; An, Y.; Yang, S. Enhancing full water-splitting performance of transition metal bifunctional electrocatalysts in alkaline solutions by tailoring CeO<sub>2</sub>–transition metal oxides–Ni nanointerfaces. *ACS Energy Lett.* **2018**, *3*, 290–296. [[CrossRef](#)]
12. Hou, Y.; Zhuang, X.; Feng, X. Recent Advances in Earth-Abundant Heterogeneous Electrocatalysts for Photoelectrochemical Water Splitting. *Small Methods* **2017**, *1*, 1700090. [[CrossRef](#)]
13. Haribal, V.P.; He, F.; Mishra, A.; Li, F. Iron-Doped BaMnO<sub>3</sub> for Hybrid Water Splitting and Syngas Generation. *ChemSusChem* **2017**, *10*, 3402–3408. [[CrossRef](#)] [[PubMed](#)]
14. Wang, W.; Xu, M.; Xu, X.; Zhou, W.; Shao, Z. Perovskite Oxide Based Electrodes for High-Performance Photoelectrochemical Water Splitting. *Angew. Chem. Int. Ed.* **2020**, *59*, 136–152. [[CrossRef](#)] [[PubMed](#)]
15. Wu, Y.; Tao, X.; Qing, Y.; Xu, H.; Yang, F.; Luo, S.; Tian, C.; Liu, M.; Lu, X. Cr-Doped FeNi–P Nanoparticles Encapsulated into N-Doped Carbon Nanotube as a Robust Bifunctional Catalyst for Efficient Overall Water Splitting. *Adv. Mater.* **2019**, *31*, e1900178. [[CrossRef](#)] [[PubMed](#)]
16. Shi, X.; Wu, A.; Yan, H.; Zhang, L.; Tian, C.; Wang, L.; Fu, H. A “MOFs plus MOFs” strategy toward Co–Mo 2 N tubes for efficient electrocatalytic overall water splitting. *J. Mater. Chem. A* **2018**, *6*, 20100–20109. [[CrossRef](#)]
17. Zhang, Y.; Fu, J.; Zhao, H.; Jiang, R.; Tian, F.; Zhang, R. Tremella-like Ni<sub>3</sub>S<sub>2</sub>/MnS with ultrathin nanosheets and abundant oxygen vacancies directly used for high speed overall water splitting. *Appl. Catal. B Environ.* **2019**, *257*, 117899. [[CrossRef](#)]
18. Zhang, Q.; Li, X.L.; Tao, B.X.; Wang, X.H.; Deng, Y.H.; Gu, X.Y.; Li, L.J.; Xiao, W.; Li, N.B.; Luo, H.Q. CoNi based alloy/oxides@N-doped carbon core-shell dendrites as complementary water splitting electrocatalysts with significantly enhanced catalytic efficiency. *Appl. Catal. B Environ.* **2019**, *254*, 634–646. [[CrossRef](#)]
19. Zhu, Q.-L.; Xu, Q. Metal–organic framework composites. *Chem. Soc. Rev.* **2014**, *43*, 5468–5512. [[CrossRef](#)]
20. Wang, S.; McGuirk, C.M.; d’Aquino, A.; Mason, J.A.; Mirkin, C.A. Metal–organic framework nanoparticles. *Adv. Mater.* **2018**, *30*, 1800202. [[CrossRef](#)]

21. Mahmood, A.; Guo, W.; Tabassum, H.; Zou, R. Metal-Organic Framework-Based Nanomaterials for Electrocatalysis. *Adv. Energy Mater.* **2016**, *6*, 1600423. [[CrossRef](#)]
22. Zhang, T.; Du, J.; Zhang, H.; Xu, C. In-situ growth of ultrathin ZIF-67 nanosheets on conductive Ti@TiO<sub>2</sub>/CdS sub-strate for high-efficient electrochemical catalysis. *Electrochim. Acta* **2016**, *219*, 623–629. [[CrossRef](#)]
23. Wang, S.; Wang, X. Multifunctional Metal-Organic Frameworks for Photocatalysis. *Small* **2015**, *11*, 3097–3112. [[CrossRef](#)]
24. Song, F.; Li, W.; Sun, Y. Metal–Organic Frameworks and Their Derivatives for Photocatalytic Water Splitting. *Inorganics* **2017**, *5*, 40. [[CrossRef](#)]
25. Jiao, L.; Wang, Y.; Jiang, H.-L.; Xu, Q. Metal-Organic Frameworks as Platforms for Catalytic Applications. *Adv. Mater.* **2018**, *30*, e1703663. [[CrossRef](#)]
26. Zhang, L.; Zhang, Y.; Huang, S.; Yuan, Y.; Li, H.; Jin, Z.; Wu, J.; Liao, Q.; Hu, L.; Lu, J.; et al. Co<sub>3</sub>O<sub>4</sub>/Ni-based MOFs on carbon cloth for flexible alkaline battery-supercapacitor hybrid devices and near-infrared photo-catalytic hydrogen evolution. *Electrochim. Acta* **2018**, *281*, 189–197. [[CrossRef](#)]
27. Abdi, F.F.; Berglund, S.P. Recent developments in complex metal oxide photoelectrodes. *J. Phys. D Appl. Phys.* **2017**, *50*, 193002. [[CrossRef](#)]
28. Zeng, L.; Guo, X.; He, C.; Duan, C. Metal–organic frameworks: Versatile materials for heterogeneous photocatalysis. *ACS Catal.* **2016**, *6*, 7935–7947. [[CrossRef](#)]
29. Pattengale, B.; Yang, S.; Lee, S.; Huang, J. Mechanistic Probes of Zeolitic Imidazolate Framework for Photocatalytic Application. *ACS Catal.* **2017**, *7*, 8446–8453. [[CrossRef](#)]
30. Wang, C.; Xie, Z.; Dekrafft, K.E.; Lin, W. Doping Metal–Organic Frameworks for Water Oxidation, Carbon Dioxide Reduction, and Organic Photocatalysis. *J. Am. Chem. Soc.* **2011**, *133*, 13445–13454. [[CrossRef](#)]
31. Lu, Q.; Yu, Y.; Ma, Q.; Chen, B.; Zhang, H. 2D Transition-Metal-Dichalcogenide-Nanosheet-Based Composites for Photocatalytic and Electrocatalytic Hydrogen Evolution Reactions. *Adv. Mater.* **2016**, *28*, 1917–1933. [[CrossRef](#)] [[PubMed](#)]
32. Najafi, M.; Di Giacomo, F.; Zhang, D.; Shanmugam, S.; Senes, A.; Verhees, W.; Hadipour, A.; Galagan, Y.; Aernouts, T.; Veenstra, S.; et al. Highly Efficient and Stable Flexible Perovskite Solar Cells with Metal Oxides Nanoparticle Charge Extraction Layers. *Small* **2018**, *14*, e1702775. [[CrossRef](#)]
33. Naqvi, S.T.R.; Shirinfar, B.; Majeed, S.; Najam-Ul-Haq, M.; Hussain, D.; Iqbal, T.; Ahmed, N.; Iqbal, T. Synthesis, design and sensing applications of nanostructured ceria-based materials. *Analyst* **2018**, *143*, 5610–5628. [[CrossRef](#)]
34. Hussain, D.; Musharraf, S.G.; Najam-ul-Haq, M. Development of diamond-lanthanide metal oxide affinity composites for the selective capture of endogenous serum phosphopeptides. *Anal. Bioanal. Chem.* **2016**, *408*, 1633–1641. [[CrossRef](#)] [[PubMed](#)]
35. Zeng, Z.; Liu, Y.; Zhang, W.; Chevva, H.; Wei, J. Improved supercapacitor performance of MnO<sub>2</sub>-electrospun carbon nanofibers electrodes by mT magnetic field. *J. Power Sources* **2017**, *358*, 22–28. [[CrossRef](#)]
36. Chikoidze, E.; Fellous, A.; Perez-Tomas, A.; Sauthier, G.; Tchelidze, T.; Ton-That, C.; Huynh, T.T.; Phillips, M.; Russell, S.; Jennings, M.; et al. P-type β-gallium oxide: A new perspective for power and optoelectronic devices. *Mater. Today Phys.* **2017**, *3*, 118–126. [[CrossRef](#)]
37. Chen, X.; Huang, Y.; Zhang, K.; Feng, X.; Wang, M. Porous TiO<sub>2</sub> nanobelts coated with mixed transition-metal oxides Sn<sub>3</sub>O<sub>4</sub> nanosheets core-shell composites as high-performance anode materials of lithium ion batteries. *Electrochim. Acta* **2018**, *259*, 131–142. [[CrossRef](#)]
38. Maeda, K.; Teramura, K.; Lu, D.; Saito, N.; Inoue, Y.; Domen, K. Noble-Metal/Cr<sub>2</sub>O<sub>3</sub> Core/Shell Nanoparticles as a Cocatalyst for Photocatalytic Overall Water Splitting. *Angew. Chem.* **2006**, *118*, 7970–7973. [[CrossRef](#)]
39. Gao, D.; Liu, R.; Biskupek, J.; Kaiser, U.; Song, Y.F.; Streb, C. Modular Design of Noble-Metal-Free Mixed Metal Oxide Electrocatalysts for Complete Water Splitting. *Angew. Chem. Int. Ed.* **2019**, *58*, 4644–4648. [[CrossRef](#)]
40. Zhang, G.; Yang, J.; Wang, H.; Chen, H.; Yang, J.; Pan, F. Co<sub>3</sub>O<sub>4-δ</sub> quantum dots as a highly efficient oxygen evolution reaction catalyst for water splitting. *ACS Appl. Mater. Interfaces* **2017**, *9*, 16159–16167. [[CrossRef](#)]
41. Diebold, U. The surface science of titanium dioxide. *Surf. Sci. Rep.* **2003**, *48*, 53–229. [[CrossRef](#)]
42. Kukovec, Á.; Kordás, K.; Kiss, J.; Kónya, Z. Atomic scale characterization and surface chemistry of metal modified titanate nanotubes and nanowires. *Surf. Sci. Rep.* **2016**, *71*, 473–546. [[CrossRef](#)]
43. Ding, H.; Zhang, X.-K.; Fan, J.-Q.; Zhan, X.-Q.; Xie, L.; Shi, D.; Jiang, T.; Tsai, F.-C. MOF-Templated Synthesis of Co<sub>3</sub>O<sub>4</sub>@TiO<sub>2</sub> Hollow Dodecahedrons for High-Storage-Density Lithium-Ion Batteries. *ACS Omega* **2019**, *4*, 13241–13249. [[CrossRef](#)] [[PubMed](#)]
44. Hussain, D.; Najam-ul-Haq, M.; Majeed, S.; Musharraf, S.G.; Lu, Q.; He, X.; Feng, Y.-Q. Facile liquid-phase deposition synthesis of titania-coated magnetic sporopollenin for the selective capture of phosphopeptides. *Anal. Bioanal. Chem.* **2019**, *411*, 3373–3382. [[CrossRef](#)]
45. Shi, Z.; Lan, L.; Li, Y.; Yang, Y.; Zhang, Q.; Wu, J.; Zhang, G.; Zhao, X. Co<sub>3</sub>O<sub>4</sub>/TiO<sub>2</sub> Nanocomposite Formation Leads to Improvement in Ultraviolet–Visible–Infrared–Driven Thermocatalytic Activity Due to Photoactivation and Photocatalysis–Thermocatalysis Synergetic Effect. *ACS Sustain. Chem. Eng.* **2018**, *6*, 16503–16514. [[CrossRef](#)]
46. Huang, H.; Li, X.; Han, X.; Tian, N.; Zhang, T. Moderate band-gap-broadening induced high separation of electron–hole pairs in Br substituted BiOI: A combined experimental and theoretical investigation. *Phys. Chem. Chem. Phys.* **2014**, *17*, 3673–3679. [[CrossRef](#)] [[PubMed](#)]